

Derivation of the anisotropy profile, constraints on the local velocity dispersion, and implications for direct detection

Daniel R. Hunter

Physics Department and The McDonnell Center for the Space Sciences, Washington University, St. Louis, MO 63130, USA

E-mail: dhunter@physics.wustl.edu

Abstract. We study the implications of a pseudo-phase-space density power-law for the anisotropy and velocity dispersion profiles of a Milky Way-like dark matter halo. Requiring that the anisotropy parameter does not take non-physical values within the virial radius places a maximum value on the local radial velocity dispersion. It is possible to take a local total velocity dispersion of up to about 275 km/s. Making this choice uniquely specifies the anisotropy and dispersion profiles. We introduce a way to model the local velocity distribution that incorporates this anisotropy and study the impact on direct detection.

Contents

1	Introduction and basic equations	1
2	Asymptotic behavior	3
3	Constraints from the anisotropy parameter	3
4	Anisotropic velocity distributions and predictions	6
5	Conclusions	9
A	General expressions	10
B	Details of anisotropic velocity distributions	11

1 Introduction and basic equations

The shape of the velocity distribution is an important influence on predictions for detection of galactic dark matter (DM) [1], both indirect [2–4] and direct [5–8]. N-body simulations tell us the mass distribution of dark matter in galactic halos, but it is more difficult to measure the velocity distribution from these data. Making assumptions about the phase-space density, one can derive the velocity distribution from a mass density profile [9]. This usually involves constraining the anisotropy profile to a certain functional form [10–13] (alternatively, see [14]). Here we *derive* the anisotropy profile using only information from models of N-body simulations and the Jeans equation (see also [15]). We assume spherical symmetry in this work (see [16] for a study of anisotropy in triaxial halos). It should also be kept in mind that while any function that satisfies the collisionless Boltzmann equation also satisfies the Jeans equation, the converse is not necessarily true.

For some years now, it has been apparent that the pseudo-phase-space density (PPSD) of simulated halos can be effectively modelled by a power-law over many decades of radius [17–19]. Some early work assumed isotropy and derived the mass distribution from this assumption [20, 21]. Work has also been done to explain the dynamical origins of such a power-law. We will study how assuming a density profile and a PPSD power-law completely specifies the dispersion profile and anisotropy profile of a halo. The sensitivity to the precise slope of the PPSD power-law will be considered. This may be important since evidence for a PPSD power-law so far comes from DM-only simulations. It is becoming viable, however, to include complicated baryonic effects in simulations, which may result in a PPSD slope so far unmeasured or erase the power-law trend completely. We focus on a Milky Way-sized DM halo, which is specified by the halo parameters: the virial mass $M_{\text{vir}} = 10^{12} \mathcal{M}_{\odot}$, the scale radius $r_s = 20$ kpc, and the concentration $c \equiv r_{\text{vir}}/r_s = 10$.

We use the Navarro, Frenk, and White (NFW) profile [22], which has mass distribution

$$\rho(x) = \frac{\rho_s}{x(1+x)^2}, \quad (1.1)$$

where ρ_s is a scale density and $x \equiv r/r_s$ is the dimensionless radius. The contained mass is

$$M(x) = 4\pi r_s^3 \rho_s \left(-\frac{x}{1+x} + \log(1+x) \right). \quad (1.2)$$

Solving for the virial mass M_{vir} gives ρ_s in terms of the halo parameters.

Following Taylor and Navarro [17], we take the PPSD to be a power-law with negative slope α :

$$\frac{\rho}{\sigma_r^3} = \frac{\rho_0}{\sigma_{r,0}^3} \left(\frac{x}{x_0} \right)^{-\alpha}. \quad (1.3)$$

Here we define x_0 so that $\gamma(x_0) = 6 - 2\alpha$, where $\gamma(x)$ is the negative log-log slope of the density (see [20] for details):

$$\gamma(x) \equiv -\frac{d \log(\rho)}{d \log(x)} \quad (1.4)$$

$$= \frac{1+3x}{1+x}. \quad (1.5)$$

Thus we have

$$x_0 = -\frac{5-2\alpha}{3-2\alpha}, \quad (1.6)$$

$$\rho_0 = \frac{\rho_s}{x_0(1+x_0)^2}. \quad (1.7)$$

The radial velocity dispersion σ_r follows:

$$\sigma_r^2(x) = \sigma_{r,0}^2 \left[\left(\frac{x_0}{x} \right)^{1-\alpha} \left(\frac{1+x_0}{1+x} \right)^2 \right]^{2/3}. \quad (1.8)$$

The constant $\sigma_{r,0}$ can be determined by assuming a local radial velocity dispersion $\sigma_{r,\odot}$.

The anisotropy parameter β is defined as

$$\beta \equiv 1 - \frac{\sigma_t^2}{2\sigma_r^2}, \quad (1.9)$$

where σ_r is the radial velocity dispersion and σ_t is the tangential velocity dispersion. From the integral Jeans equation [9], we can solve for the anisotropy parameter (compare with [15, 23]):

$$\beta(x) = \frac{5}{6}\gamma(x) - \frac{\alpha}{3} - \frac{GM(x)}{2xr_s\sigma_r^2(x)}. \quad (1.10)$$

Specific to the case of the NFW profile, this is

$$\beta(x) = \frac{5+15x}{6+6x} - \frac{\alpha}{3} - B_0 x^{-(2\alpha+1)/3} (1+x)^{1/3} [-x + (1+x)\log(1+x)]. \quad (1.11)$$

We have introduced the factor B_0 , which collects all of the halo parameters and is defined as

$$B_0 \equiv \frac{2\pi G r_s^2 \rho_s}{\sigma_{r,0}^2} \left[x_0^{1-\alpha} (1+x_0)^2 \right]^{-2/3}. \quad (1.12)$$

See Appendix A for more general expressions of several of the above quantities.

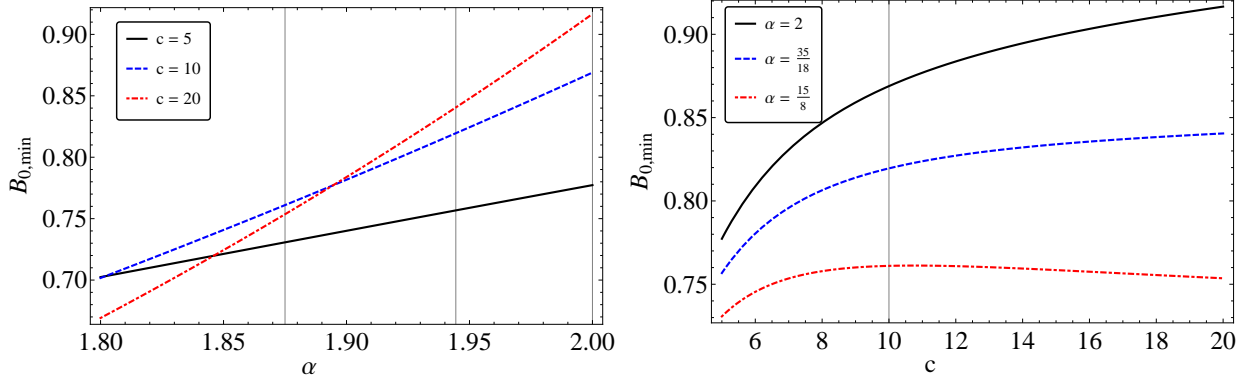


Figure 1: Minimum values of B_0 as a function of the PPSD slope or halo concentration. Vertical grid lines denote typical values for the PPSD slope or the chosen value for the DM halo concentration.

2 Asymptotic behavior

We split the function for the anisotropy parameter into two parts, so $\beta(x) = A(x) + B(x)$, with

$$A(x) = \frac{5 + 15x}{6 + 6x} - \frac{\alpha}{3}, \quad (2.1)$$

$$B(x) = -B_0 x^{-(2\alpha+1)/3} (1+x)^{1/3} [-x + (1+x) \log(1+x)]. \quad (2.2)$$

The first part has simple asymptotic limits

$$A(x) \rightarrow \begin{cases} (5 - 2\alpha)/6 & \text{for } x \rightarrow 0 \\ (15 - 2\alpha)/6 & \text{for } x \rightarrow \infty \end{cases} \quad (2.3)$$

while the second is more complicated. In the limit $x \rightarrow 0$, we have

$$B(x) \rightarrow \begin{cases} -\infty & \text{if } \alpha > 5/2 \\ -B_0/2 & \text{if } \alpha = 5/2 \\ 0 & \text{if } \alpha < 5/2 \end{cases} \quad (2.4)$$

and in the limit $x \rightarrow \infty$, we have

$$B(x) \rightarrow \begin{cases} 0 & \text{if } \alpha > 3/2 \\ -\infty & \text{if } \alpha \leq 3/2 \end{cases} \quad (2.5)$$

3 Constraints from the anisotropy parameter

We see from eq. (2.3) and (2.5) that $A(x)$ always dominates at extreme values of x for $\alpha \approx 2$. This is acceptable in the small- x limit, where $\beta \rightarrow 1/6$ for, as an example, $\alpha = 2$. However, in the large- x limit, with the same value of α , $\beta \rightarrow 11/6$, which is greater than one, implying an

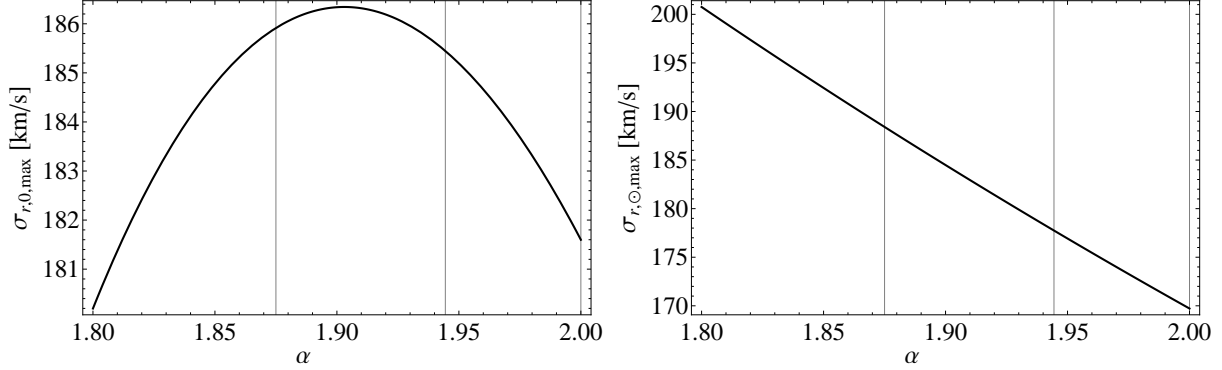


Figure 2: Maximum values of the parameter $\sigma_{r,0}$ and of the local radial velocity dispersion $\sigma_{r,\odot}$.

imaginary velocity dispersion. Requiring that $\beta \leq 1$ as $x \rightarrow \infty$ would imply $\alpha \geq 9/2$, which is a far greater slope than seen in simulations. This unphysical behavior may suggest that we cannot have a physical model that simultaneously exhibits an NFW density profile and power-law PPSD, but let us suppose that this requirement for physical-ness is too restrictive. Instead, let us just require that the anisotropy parameter is no greater than one everywhere within the virial radius.

Mathematically, we require

$$\forall x \leq c : \beta(x) \leq 1. \quad (3.1)$$

We can effectively satisfy this for our purposes by requiring that $\beta(c) \leq 1$. This gives a minimum value for B_0 :

$$B_0 \geq \frac{c^{(1+2\alpha)/3} [9c - 2\alpha(1+c) - 1]}{6(1+c)^{4/3} [(1+c) \log(1+c) - c]}. \quad (3.2)$$

The constraint on B_0 depends only on the concentration (by way of the virial mass) and PPSD log-slope α . The minimum value of B_0 is plotted versus each parameter for representative values of the other in Figure 1. From the definition of B_0 in eq. (1.12), this immediately gives an *upper* bound on $\sigma_{r,0}$ and thus also on $\sigma_{r,\odot}$ (see eq. (1.8)). These are plotted in Figure 2. Once $\sigma_{r,\odot}$ is set the anisotropy profile $\beta(x)$ is totally specified. In Figure 3 we plot the local anisotropy parameter $\beta_\odot = \beta(x_\odot)$ and the local *total* velocity dispersion $\sigma_{\text{tot},\odot}$ versus the choice of $\sigma_{r,\odot}$, using the relation $\sigma_{\text{tot},\odot}^2 = (3 - 2\beta_\odot)\sigma_{r,\odot}^2$. We see that $\sigma_{\text{tot},\odot}$ depends monotonically on the choice of $\sigma_{r,\odot}$, so we immediately also have an upper bound on $\sigma_{\text{tot},\odot}$, which is shown in Figure 4.

We proceed with two general cases. The first is the “conservative” case, in which we set $\sigma_{r,\odot}$ so that $\sigma_{\text{tot},\odot} = 220$ km/s, the local circular velocity in the galaxy (see Figure 3). The second is the “extreme” case, in which we set $\sigma_{r,\odot}$ to its maximum allowed value (see Figure 2), which results in $\sigma_{\text{tot},\odot}$ being about 260 to 275 km/s.

The radial velocity dispersion profiles for the two cases are plotted in Figure 5, and the total velocity dispersion profiles are plotted in Figure 6. We also plot the solution for the isotropic (*i.e.* $\beta = 0$ everywhere) NFW case. The same halo parameters (M_{vir} , r_s , and c) are used to plot the dispersion in the isotropic case, but there is no freedom to also specify the local (total or radial) dispersion, since the anisotropy has been constrained to zero everywhere.

Finally, we plot the anisotropy profiles in Figure 7. Generally, in the conservative case, the profile is slightly radially biased near the center, reaches a minimum at around a tenth the scale

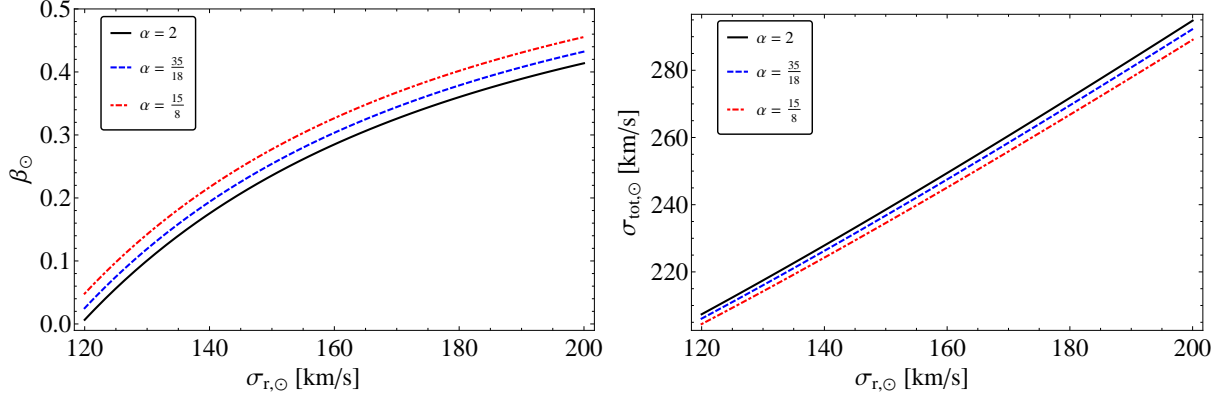


Figure 3: Choosing a value for the local radial velocity dispersion, which is constrained as shown in Figure 2, fixes the values of the local total velocity dispersion and the local anisotropy.

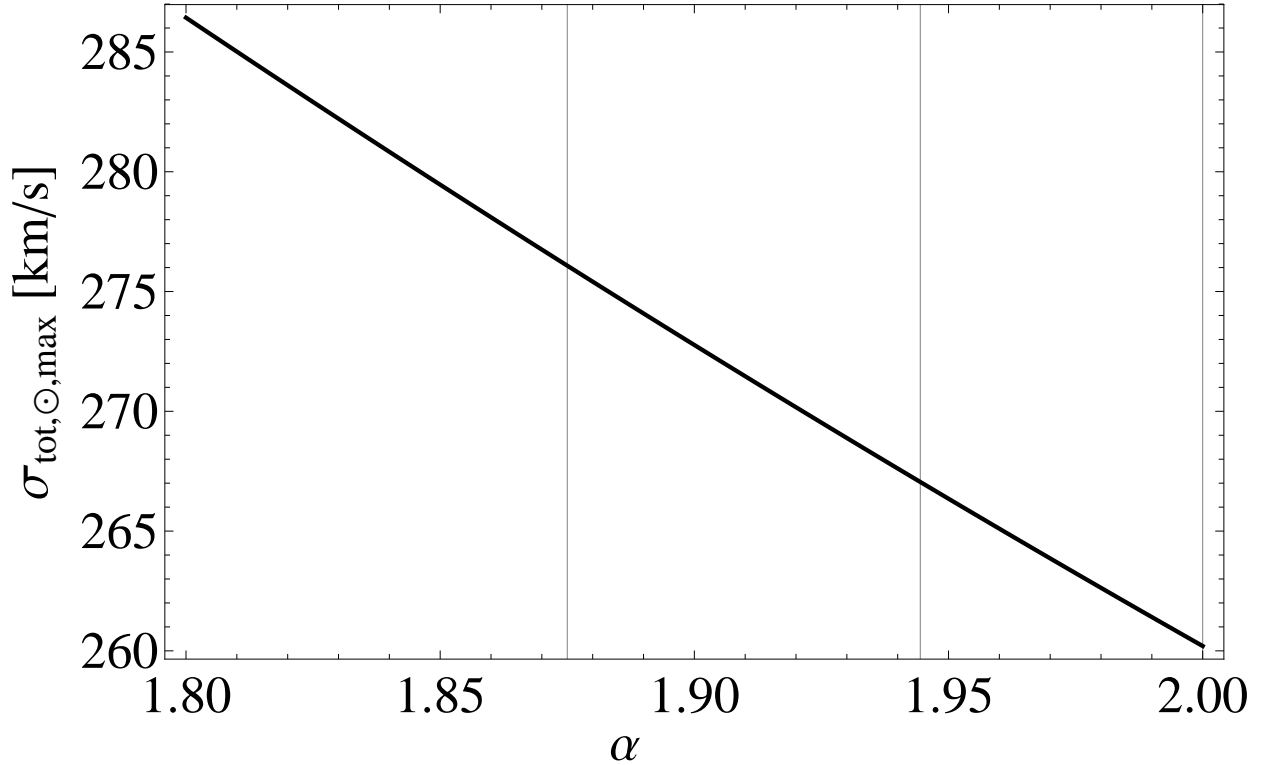


Figure 4: Maximum values of the local total velocity dispersion $\sigma_{\text{tot},\odot}$, determined from Figures 2 and 3.

radius, and rises to a (local) maximum of around 0.4 to 0.6 before the virial radius. We see in all cases that the anisotropy parameter rises slowly to the value in eq. (2.3) for $x \rightarrow 0$. See [24] for a discussion of central anisotropy. Here we do not presume that either assumed model, of the

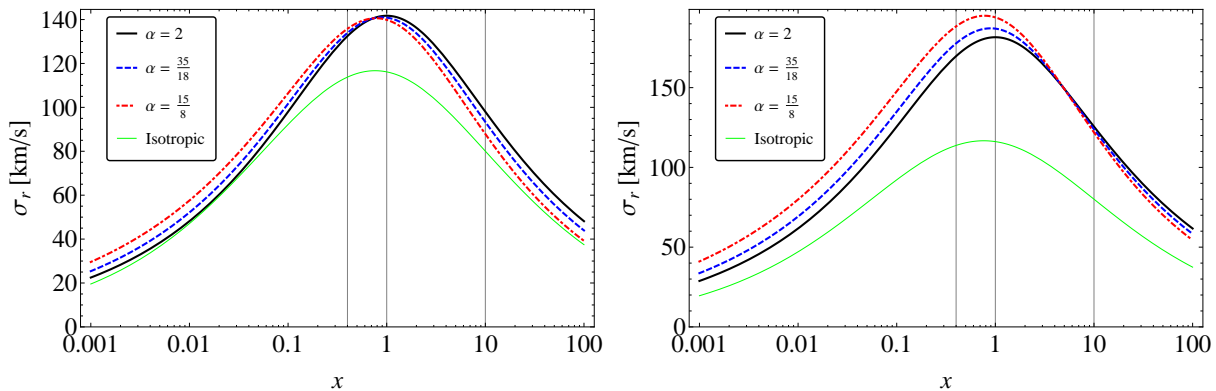


Figure 5: The radial velocity dispersion σ_r as a function of radius, in units of the scale radius, for a few values of the PPSD slope. The left plot shows the conservative case, and the right plot shows the extreme case, as described in the text. The isotropic dispersion profile is also shown and is determined entirely by the halo parameters. Vertical grid lines denote the local radius, scale radius, and virial radius.

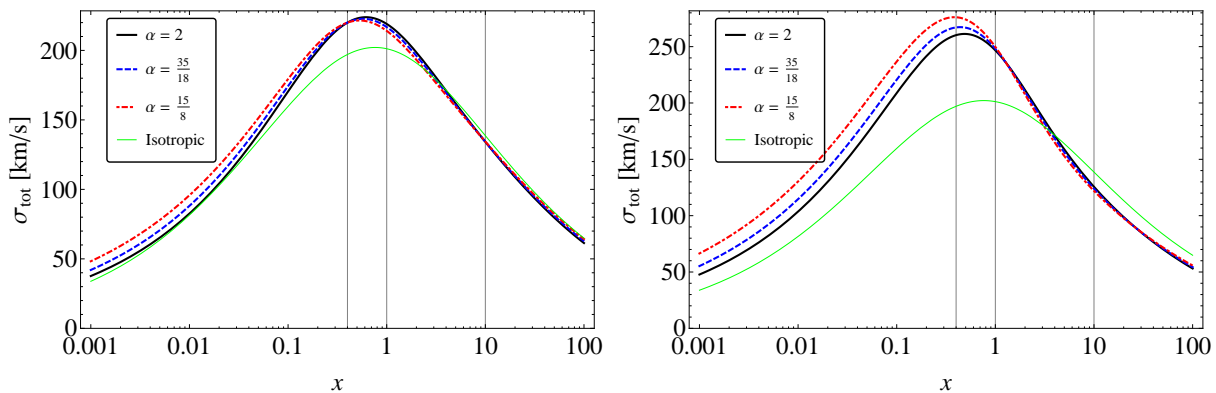


Figure 6: Same as in Figure 5, but for the total velocity dispersion σ_{tot} .

mass distribution or PPSD, necessarily stays valid at very small or very large radii. See [25] for an investigation of the break-down of the PPSD power law.

4 Anisotropic velocity distributions and predictions

Recently, close attention has been paid to the form of the velocity distribution used to calculate predictions for indirect and direct DM detection. The standard halo model no longer suffices [26] and in some cases the functional form of the distribution can make a significant difference. Especially, the assumed velocity distribution influences the interpretation of results from direct detection experiments [7, 27, 28]. We introduce a new, anisotropic generalization of the model proposed by

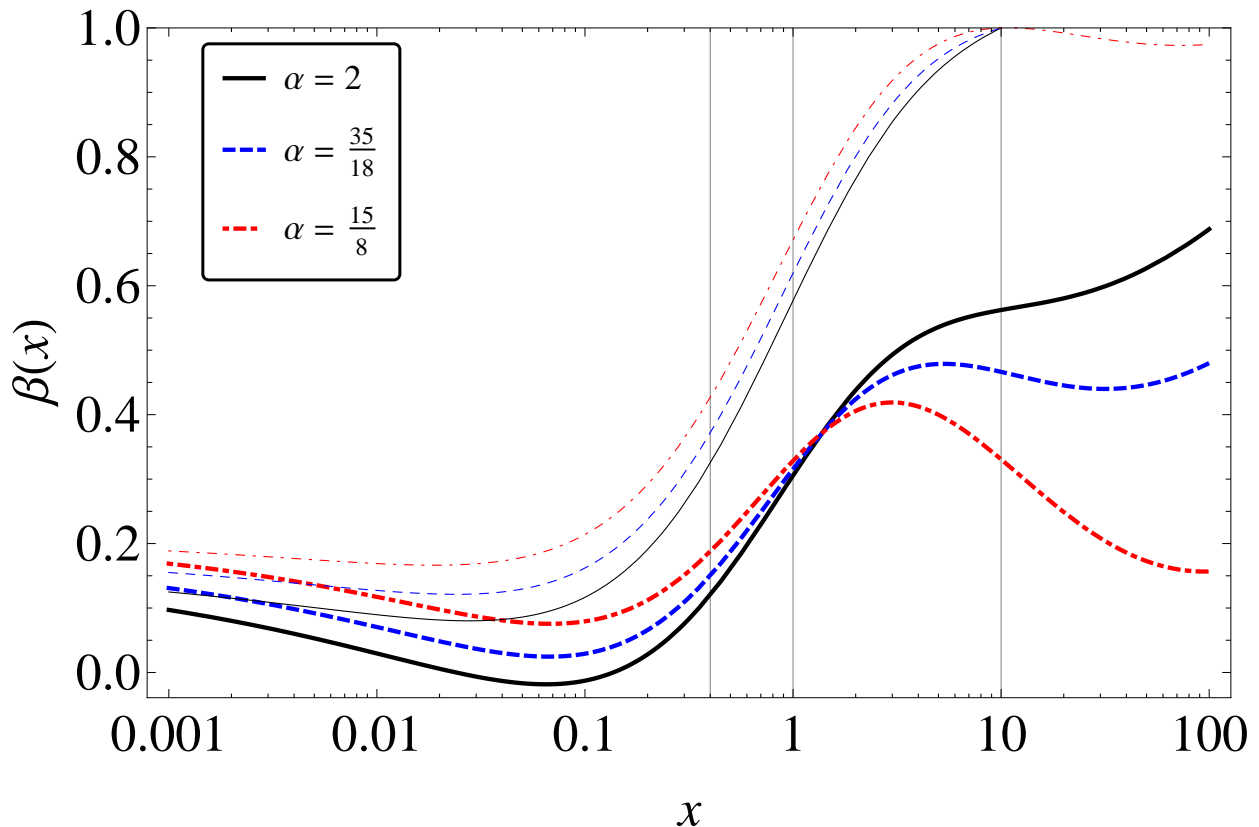


Figure 7: The anisotropy profile for the conservative case (thick lines) and the extreme case (thin lines). Grid lines designate the local, scale, and virial radii.

Mao, et al. [29]:

$$f(\mathbf{v}) \propto \exp \left\{ -\sqrt{\frac{v_r^2}{v_{r,0}^2} + \frac{v_t^2}{v_{t,0}^2}} \right\} (v_{\text{esc}}^2 - v^2)^p, \quad (4.1)$$

where $v_r = v \cos(\eta)$ and $v_t = v \sin(\eta)$ are the radial and tangential velocity components and η is the angle from the radial direction. The parameters $v_{r,0}$ and $v_{t,0}$ are not dispersions but just velocity scales. The exponent p characterizes the high-velocity tail. The function is normalized so that $\int d\mathbf{v} f(\mathbf{v}) = 1$. We choose this distribution because of its recent success in modeling the Eris simulation (see Fig. 3 in [30]). For consistency with that study, we take $p = 2.7$. The escape speed v_{esc} is not a parameter, but is given by $\sqrt{-2\Phi}$, where Φ is the gravitational potential, which we calculate from the density profile, assuming a solar radius of 8 km. The total dispersion σ_{tot} and the anisotropy parameter β are then determined by the parameters $v_{r,0}$ and $v_{t,0}$. We recover the original, isotropic distribution when $v_{r,0} = v_{t,0}$. See Appendix B for details on the selection of values for $v_{r,0}$ and $v_{t,0}$.

We use the function in eq. (4.1) to model the local velocity distribution with the intention

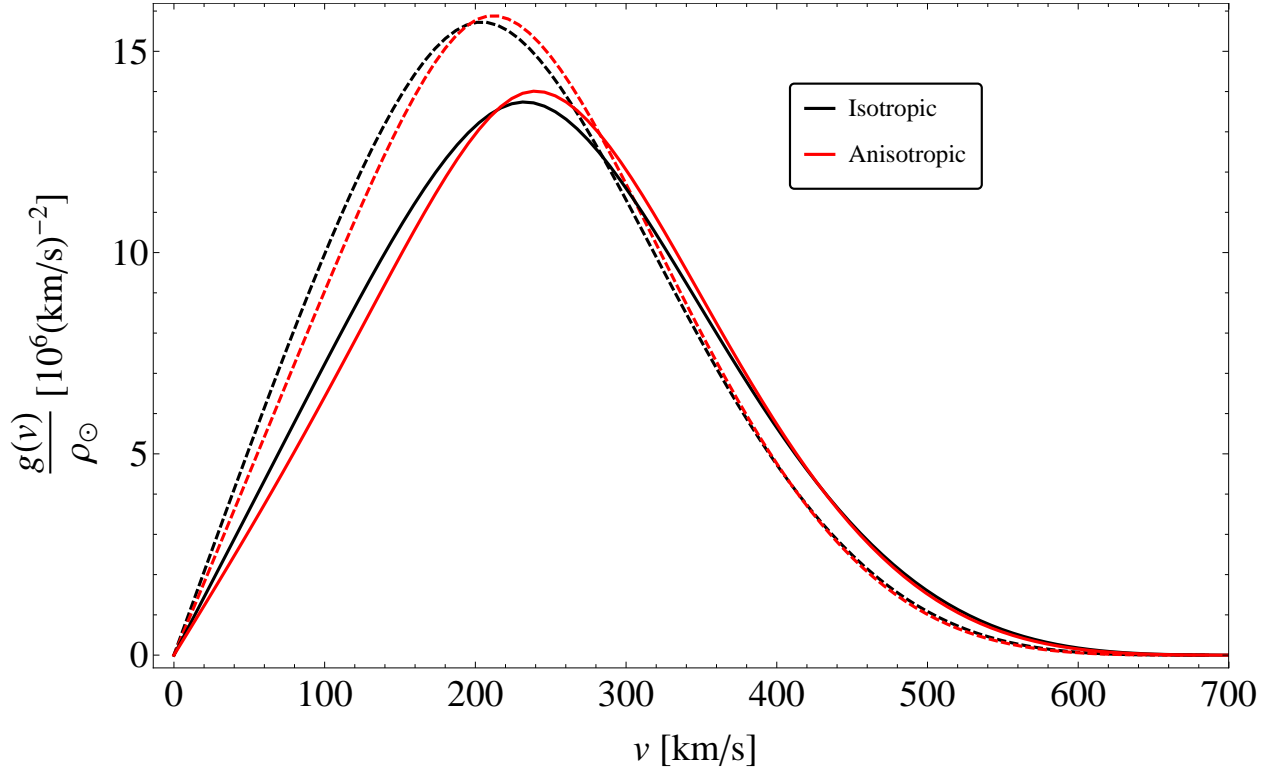


Figure 8: The function $g(v_{\text{th}})$ defined in eq. (4.2). Solid lines are calculated in June; dashed lines are calculated in December.

of understanding the impact that anisotropy can have on direct detection. For the purposes of this work, we assume a conservative value of 0.2 for the local anisotropy parameter β_{\odot} . It is straight-forward to calculate the function

$$g(v, t) = \rho_{\odot} \int_0^{\pi} d\eta \sin(\eta) \int_0^{2\pi} d\psi v f(\mathbf{v}_{\text{halo}}), \quad (4.2)$$

where \mathbf{v}_{halo} is the velocity vector boosted from the detector frame to the halo frame [7]. The boost depends on the time of the year t . In Figure 8 we plot this function for June and December; for the isotropic case and the anisotropic case. Using the function $g(v_{\text{th}}, t)$, the differential detection rate is found by specifying a velocity threshold v_{th} for DM particles in the detector frame:

$$\frac{dR}{dQ} \propto G(v_{\text{th}}, t) \equiv \int_{v \geq v_{\text{th}}} dv g(v, t). \quad (4.3)$$

The velocity threshold is determined by the specifics of any particular experiment and the DM particle mass, and we leave it free. Figure 9 plots the function G , averaged between June and December, for the isotropic and anisotropic cases, with the fractional difference

$$\Delta G = (G_{\text{Ani}} - G_{\text{Iso}}) / G_{\text{Iso}}. \quad (4.4)$$

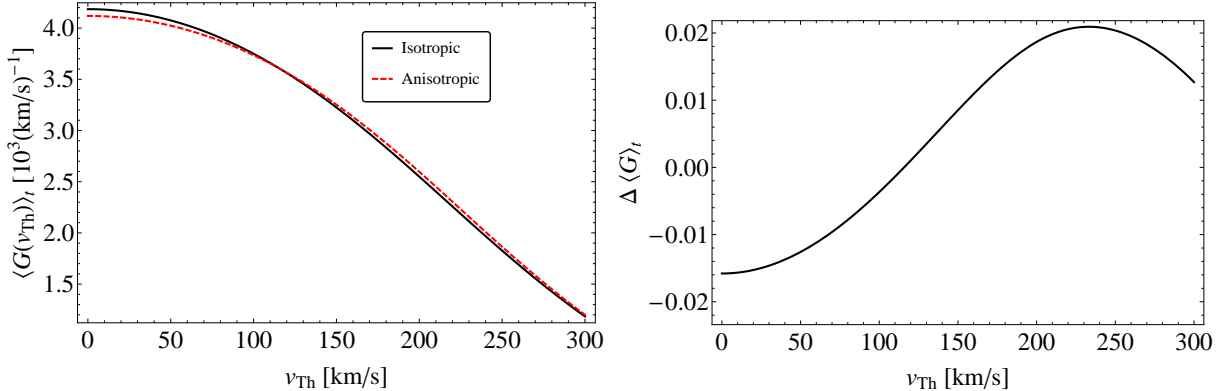


Figure 9: The time-averaged function $\langle G(v_{\text{th}}, t) \rangle_t$ as a function of the velocity threshold (see eq. (4.3)) and the fractional difference between the isotropic to anisotropic cases.

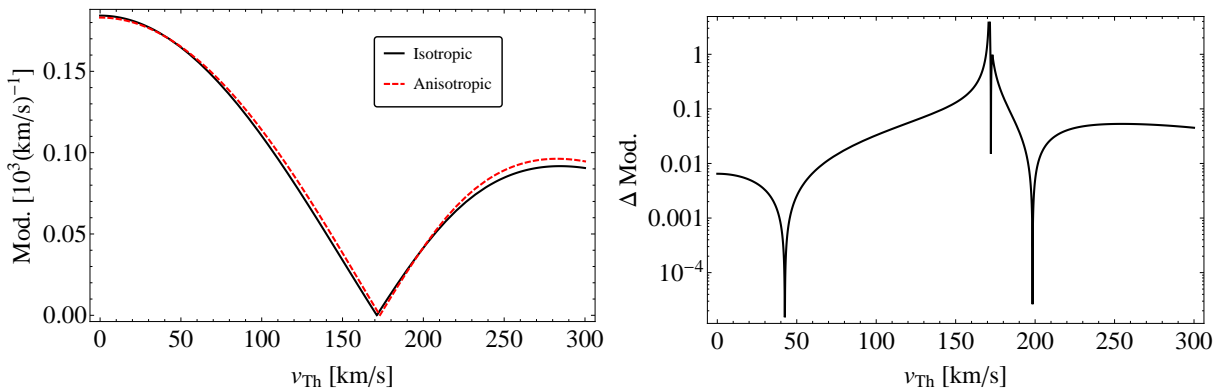


Figure 10: Signal modulation amplitude as a function of the velocity threshold and the fractional difference between the isotropic to anisotropic cases. The jagged area at $v_{\text{th}} \approx 170$ km/s is around where the modulation amplitudes each go to zero.

We also consider the modulation amplitude of the signal, defined here as half the difference between the rate in June and the rate in December:

$$A(v_{\text{th}}) = |G(v_{\text{th}}, t_{\text{June}}) - G(v_{\text{th}}, t_{\text{Dec}})|/2. \quad (4.5)$$

This is plotted in Figure 10 for the isotropic and anisotropic cases, with the fractional difference, analogous to eq. (4.4).

5 Conclusions

Combining models of the mass distribution and pseudo-phase-space density, the Jeans equation gives us a particular anisotropy profile. Requiring this profile to be physical inside the virial radius implies a maximum value for the local velocity dispersion. We have used an anisotropic modification to the model proposed by Mao et al. [29], which was also used to model the Eris simulation. We

find that assuming a local anisotropy of approximately 0.2 is reasonable and conservative. In the Eris simulation, a comparable amount of radially biased anisotropy was found at the location corresponding to the solar radius (see Fig. 2 in [30]).

Different direct detection collaborations have found contradictory results (*e.g.* see [31]). Part of the general goal in studying the local velocity distribution is to alleviate these discrepancies. Since different experiments can have different threshold velocities, Figure 9 suggests that the difference between observed signals can vary by almost 4% due to the effect of local anisotropy. This may seem small, but it is comparable to the uncertainty introduced by considering different density profiles [7]. The modification to the modulation amplitude can be even more significant and is sensitive to the value of the velocity threshold, but the signal itself is smallest where the modification is greatest.

In principle, a detector that can give information about the direction of a detected WIMP's velocity would allow us to *measure* the local anisotropy. This is difficult, as it would require an individual WIMP to interact multiple times inside the detector or require a low detector density so the recoiled particle can be tracked. Once a discovery is confirmed, however, it may be viable to consider such an experiment. Future work will consider this possibility (also, see [5]).

We note that the anisotropy at radii beyond about the scale radius is sensitive to the shape of the PPSD profile and the local velocity dispersion, and it can also be fairly large. It seems unlikely that this grants a viable observational effect, since the density is so low there. Future work will, however, consider this and other implications for indirect detection, which would be influenced by anisotropy throughout the entire halo.

Acknowledgments

The author is grateful to Francesc Ferrer and Stanley D. Hunter for advice and discussions. This work was supported by the U.S. DOE at Washington University in St. Louis.

Note added: While this work was being completed, there appeared a similar study by Bozorgnia, Catena, and Schwetz [32], who find similar conclusions.

A General expressions

Here we discuss the derivation of the anisotropy parameter more generally. We consider two-power-law density profiles, with inner slope γ_0 and outer slope γ_∞ ,

$$\rho_{\gamma_0\gamma_\infty}(x) = \rho_s x^{-\gamma_0} (1+x)^{-\gamma_\infty+\gamma_0}. \quad (\text{A.1})$$

The contained mass is, omitting the constant factor $4\pi\rho_s r_s^3$,

$$M_{\gamma_0\gamma_\infty}(x) = (-1)^{\gamma_0-1} B_{-x}(3-\gamma_0, 1+\gamma_0-\gamma_\infty), \quad (\text{A.2})$$

where $B_z(a, b)$ is the incomplete beta function. Note the following particular cases:

$$M_{1\gamma_\infty}(x) = \frac{1 - [1 - x(2 - \gamma_\infty)](1 + x)^{2-\gamma_\infty}}{(3 - \gamma_\infty)(2 - \gamma_\infty)}, \quad (\text{A.3})$$

$$M_{12}(x) = x - \log(1 + x), \quad (\text{A.4})$$

$$M_{13}(x) = -\frac{x}{1 + x} + \log(1 + x), \quad (\text{A.5})$$

$$M_{\gamma_0 4}(x) = \frac{1}{3 - \gamma_0} \left(\frac{x}{1 + x} \right)^{3-\gamma_0}. \quad (\text{A.6})$$

Using the PPSD power-law in eq. (1.3), recalling that $\gamma(x_0) = 6 - 2\alpha$, we have

$$x_0 = -\frac{6 - 2\alpha - \gamma_0}{6 - 2\alpha - \gamma_\infty}, \quad (\text{A.7})$$

$$\rho_0 = \frac{\rho_s}{x_0^{\gamma_0}(1 + x_0)^{\gamma_\infty - \gamma_0}}. \quad (\text{A.8})$$

Generalizing eq. (1.8), we have the radial velocity dispersion

$$\sigma_r^2(x) = \sigma_{r,0}^2 \left[\left(\frac{x}{x_0} \right)^{\alpha - \gamma_0} \left(\frac{1 + x}{1 + x_0} \right)^{-\gamma_\infty + \gamma_0} \right]^{2/3}. \quad (\text{A.9})$$

Generalizing eq. (1.12), the constant factor B_0 is now

$$B_0 \equiv \frac{2\pi Gr_s^2 \rho_s}{\sigma_{r,0}^2} [x_0^{\alpha - \gamma_0} (1 + x_0)^{-\gamma_\infty + \gamma_0}]^{2/3}. \quad (\text{A.10})$$

The expression for the anisotropy parameter $\beta(x)$ in eq. (1.10) is general.

B Details of anisotropic velocity distributions

We use the velocity distribution in eq. (4.1) to model the local velocity distribution. The choice of parameters $v_{r,0}$ and $v_{t,0}$ determine the velocity dispersion and anisotropy parameter. Figure 11 plots contours that give the specified value of β or σ_{tot} . In this work we choose $\sigma_{\text{tot},\odot} = 220$ km/s. For the isotropic case, this implies $v_{r,0} = v_{t,0} = 164.5$ km/s; for the anisotropic case, with $\beta = 0.2$, this implies $v_{r,0} = 212.2$ km/s and $v_{t,0} = 146.6$ km/s.

References

- [1] G. Bertone, D. Hooper, and J. Silk, *Particle dark matter: Evidence, candidates and constraints*, *Phys.Rept.* **405** (2005) 279–390, [[hep-ph/0404175](#)].
- [2] B. Robertson and A. Zentner, *Dark Matter Annihilation Rates with Velocity-Dependent Annihilation Cross Sections*, *Phys.Rev.* **D79** (2009) 083525, [[arXiv:0902.0362](#)].
- [3] S. Campbell, B. Dutta, and E. Komatsu, *Effects of Velocity-Dependent Dark Matter Annihilation on the Energy Spectrum of the Extragalactic Gamma-ray Background*, *Phys.Rev.* **D82** (2010) 095007, [[arXiv:1009.3530](#)].

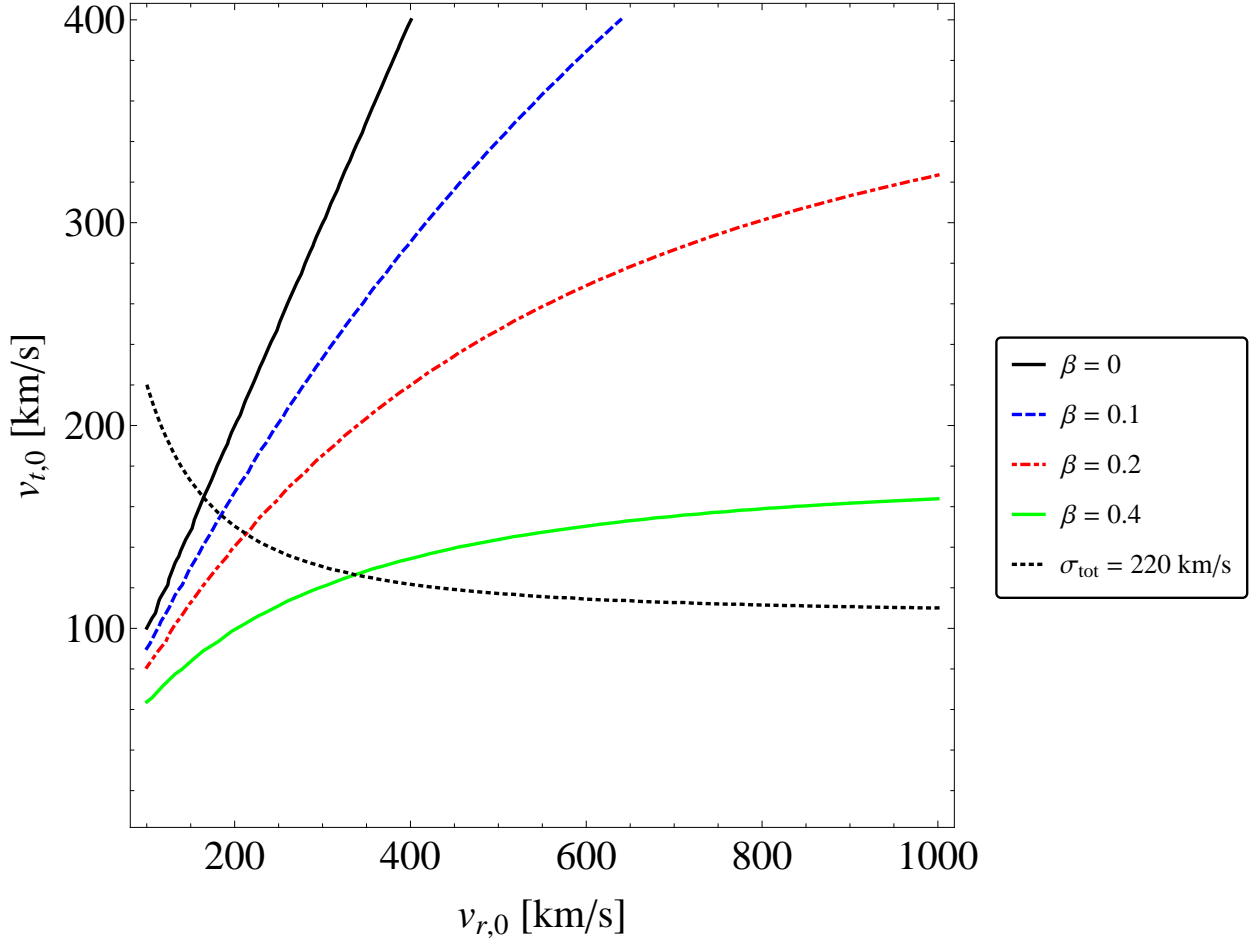


Figure 11: Contours of the parameters $v_{r,0}$ and $v_{t,0}$ that give the specified values of the anisotropy parameter or total velocity dispersion.

- [4] F. Ferrer and D. R. Hunter, *The impact of the phase-space density on the indirect detection of dark matter*, *JCAP* **1309** (2013) 005, [[arXiv:1306.6586](#)].
- [5] P. Gondolo, *Recoil momentum spectrum in directional dark matter detectors*, *Phys.Rev.* **D66** (2002) 103513, [[hep-ph/0209110](#)].
- [6] L. E. Strigari and R. Trotta, *Reconstructing WIMP Properties in Direct Detection Experiments Including Galactic Dark Matter Distribution Uncertainties*, *JCAP* **0911** (2009) 019, [[arXiv:0906.5361](#)].
- [7] R. Catena and P. Ullio, *The local dark matter phase-space density and impact on WIMP direct detection*, *JCAP* **1205** (2012) 005, [[arXiv:1111.3556](#)].
- [8] M. T. Frandsen, F. Kahlhoefer, C. McCabe, S. Sarkar, and K. Schmidt-Hoberg, *Resolving astrophysical uncertainties in dark matter direct detection*, *JCAP* **1201** (2012) 024, [[arXiv:1111.0292](#)].
- [9] J. Binney and S. Tremaine, *Galactic Dynamics: Second Edition*. Princeton University Press, 2008.

- [10] L. P. Osipkov, *Spherical systems of gravitating bodies with an ellipsoidal velocity distribution*, *Soviet Astronomy Letters* **5** (1979) 42–44.
- [11] P. Cuddeford, *An analytic inversion for anisotropic spherical galaxies*, *MNRAS* **253** (Dec., 1991) 414–426.
- [12] O. E. Gerhard, *A new family of distribution functions for spherical galaxies*, *MNRAS* **250** (June, 1991) 812–830.
- [13] M. Baes and H. Dejonghe, *The Hernquist model revisited: Completely analytical anisotropic dynamical models*, *Astron.Astrophys.* **393** (2002) 485–498, [[astro-ph/0207233](#)].
- [14] E. Van Hese, M. Baes, and H. Dejonghe, *On the universality of the global slope – anisotropy inequality*, *Astrophys.J.* **726** (2011) 80, [[arXiv:1010.4301](#)].
- [15] A. Zait, Y. Hoffman, and I. Shlosman, *Dark Matter Halos: Velocity Anisotropy – Density Slope Relation*, [arXiv:0711.3791](#).
- [16] M. Sparre and S. H. Hansen, *The behaviour of shape and velocity anisotropy in dark matter haloes*, *JCAP* **1210** (2012) 049, [[arXiv:1210.2392](#)].
- [17] J. E. Taylor and J. F. Navarro, *The Phase - space density profiles of cold dark matter halos*, *Astrophys.J.* **563** (2001) 483–488, [[astro-ph/0104002](#)].
- [18] E. Van Hese, M. Baes, and H. Dejonghe, *The dynamical structure of dark matter halos with universal properties*, *Astrophys.J.* **690** (2009) 1280–1291, [[arXiv:0809.0901](#)].
- [19] C.-P. Ma, P. Chang, and J. Zhang, *Is the Radial Profile of the Phase-Space Density of Dark Matter Halos a Power-Law?*, [arXiv:0907.3144](#).
- [20] W. Dehnen and D. McLaughlin, *Dynamical insight into dark-matter haloes*, *Mon.Not.Roy.Astron.Soc.* **363** (2005) 1057–1068, [[astro-ph/0506528](#)].
- [21] C. G. Austin, L. L. Williams, E. I. Barnes, A. Babul, and J. J. Dalcanton, *Semi-analytical dark matter halos and the Jeans equation*, *Astrophys.J.* **634** (2005) 756–774, [[astro-ph/0506571](#)].
- [22] J. F. Navarro, C. S. Frenk, and S. D. White, *A Universal density profile from hierarchical clustering*, *Astrophys.J.* **490** (1997) 493–508, [[astro-ph/9611107](#)].
- [23] K. B. Schmidt, S. H. Hansen, J. H. An, L. L. Williams, and A. V. Macci'o, *Dark Matter Angular Momentum Profile from the Jeans Equation*, *Astrophys.J.* **694** (2009) 893–901, [[arXiv:0901.0928](#)].
- [24] J. H. An and N. W. Evans, *A theorem on central velocity dispersions*, *Astrophys.J.* **701** (2009) 1500–1505, [[arXiv:0906.3673](#)].
- [25] A. D. Ludlow, J. F. Navarro, M. Boylan-Kolchin, V. Springel, A. Jenkins, et al., *The density and pseudo-phase-space density profiles of cold dark matter haloes*, *Mon.Not.Roy.Astron.Soc.* **415** (2011) 3895–3902, [[arXiv:1102.0002](#)].
- [26] S. Kazantzidis, J. Magorrian, and B. Moore, *Generating equilibrium dark matter halos: Inadequacies of the local Maxwellian approximation*, *Astrophys.J.* **601** (2004) 37–46, [[astro-ph/0309517](#)].
- [27] P. Ullio and M. Kamionkowski, *Velocity distributions and annual modulation signatures of weakly interacting massive particles*, *JHEP* **0103** (2001) 049, [[hep-ph/0006183](#)].
- [28] M. Vogelsberger, A. Helmi, V. Springel, S. D. White, J. Wang, et al., *Phase-space structure in the local dark matter distribution and its signature in direct detection experiments*, *Mon.Not.Roy.Astron.Soc.* **395** (2009) 797–811, [[arXiv:0812.0362](#)].
- [29] Y.-Y. Mao, L. E. Strigari, R. H. Wechsler, H.-Y. Wu, and O. Hahn, *Halo-to-Halo Similarity and Scatter in the Velocity Distribution of Dark Matter*, *Astrophys.J.* **764** (2013) 35, [[arXiv:1210.2721](#)].

- [30] M. Kuhlen, A. Pillepich, J. Guedes, and P. Madau, *The Distribution of Dark Matter in the Milky Way's Disk*, [arXiv:1308.1703](#).
- [31] P. Gondolo and G. B. Gelmini, *Halo independent comparison of direct dark matter detection data*, *JCAP* **1212** (2012) 015, [[arXiv:1202.6359](#)].
- [32] N. Bozorgnia, R. Catena, and T. Schwetz, *Anisotropic dark matter distribution functions and impact on WIMP direct detection*, [arXiv:1310.0468](#).